Journal of The
Electrochemical Society

OPEN ACCESS

Modeling the Effect of Over-discharge Cycling on Li-ion Batteries

To cite this article: Raghav Sai Thiagarajan *et al* 2025 *J. Electrochem. Soc.* **172** 050534

View the article online for updates and enhancements.

You may also like

- Failure Study of Commercial LiFePO$_4$ Cells in over-Discharge Conditions Using Electrochemical Impedance Spectroscopy
  Yadong Liu, Qi Liu, Zhefei Li et al.
- Detection of Over-Discharged Nickel Cobalt Aluminum Oxide Lithium Ion Cells Using Electrochemical Impedance Spectroscopy and Differential Voltage Analysis
  Norihiro Togasaki, Tokihiko Yokoshima and Tetsuya Osaka
- Degradation in lithium ion battery current collectors
  Liya Guo, Daisy B Thornton, Mohamed A Koronfel et al.

ECC-Opto-10 Optical Battery Test Cell:
Visualize the Processes Inside Your Battery!

EL-CELL®
electrochemical test equipment

✓ **Battery Test Cell for Optical Characterization**
Designed for light microscopy, Raman spectroscopy and XRD.

✓ **Optimized, Low Profile Cell Design (Device Height 21.5 mm)**
Low cell height for high compatibility, fits on standard samples stages.

✓ **High Cycling Stability and Easy Handling**
Dedicated sample holders for different electrode arrangements included!

✓ **Cell Lids with Different Openings and Window Materials Available**

Scan me!

Contact us:
☎ +49 40 79012-734
sales@el-cell.com
www.el-cell.com

Sample Test (Side-by-Side Setup)
Sample Test (Face-to-Face Setup)

This content was downloaded from IP address 128.62.251.166 on 05/06/2025 at 20:14

Journal of The Electrochemical Society, 2025 **172** 050534

Modeling the Effect of Over-discharge Cycling on Li-ion Batteries

Raghav Sai Thiagarajan,[1,=,*] **Anthony Concepción,**[2,=] **Deepti Tewari,**[3,*] **Judith A. Jeevarajan,**[3,*] **Vinay Premnath,**[3] **and Venkat R. Subramanian**[1,2,4,**,z]

[1] *Materials Science and Engineering Program, Texas Materials Institute, The University of Texas at Austin, Austin, Texas 78712, United States of America*
[2] *Walker Department of Mechanical Engineering & Material Science Engineering, Texas Materials Institute, The University of Texas at Austin, Austin, Texas 78712, United States of America*
[3] *Electrochemical Safety Research Institute, UL Research Institutes, 5000 Gulf Fwy, UHTB, Houston, Texas, 77204, United States of America*
[4] *Affiliate Faculty, Oden Institute for Computational Science and Engineering, The University of Texas at Austin, Austin, Texas 78712, United States of America*

Off-nominal circumstances inducing cell over-discharge in a battery are of concern due to electrolyte decomposition and prolonged degradation effects. Copper dissolution and its subsequent deposition could lead to high cell temperatures and, in some cases, catastrophic failures during the battery's operational lifetime. Extending physics-based lithium-ion battery models for the purpose of simulating over-discharge conditions require key considerations in model parameters, constitutive equations, and the state of charge window of operation. This paper reports a reduced-order model for over-discharge and simulating its effect under various scenarios using a thermal tanks-in-series (TTiS) approach. The model was used to compare voltage-time behavior and capacity fade during cycling for different over-discharge cycling protocols. The efficacy of cycling simulations was validated with experimental data, and the TTiS model demonstrates reasonable agreement with the voltage, temperature, and capacity fade trends under the given experimental cycling regimes.
[DOI: 10.1149/1945-7111/add775]

Manuscript submitted December 19, 2024; revised manuscript received February 27, 2025. Published June 4, 2025.

List of Symbols

Dependent Variables	
c	Electrolyte Concentration
c^s	Solid Phase Concentration
ϕ_l	Liquid Phase Potential
ϕ_s	Solid Phase Potential
T	Temperature
Other Symbols	
V_{cell}	Cell Voltage
j	Pore-wall flux
N	Electrolyte molar flux
q	Heat flux
Q_{rev}	Reversible volumetric heat generation rate
Q_{irrev}	Irreversible volumetric heat generation rate due to interfacial polarization
Q_{ohmic}	Volumetric heat generation rate due to ohmic drop
h	Ambient heat transfer coefficient
Capacity fade Symbols	
j_{sei}	SEI pore-wall flux
j_{cei}	CEI pore-wall flux
j_{pl}	Lithium Plating pore-wall flux
j_{Cu}	Copper dissolution pore-wall flux
η_{Cu}	SEI mechanism overpotential
η_{CEI}	CEI mechanism overpotential
η_{Pl}	Li Plating mechanism overpotential
η_{Cu}	Copper dissolution mechanism overpotential
κ_{SEI}	SEI layer conductivity
Other Superscripts	
surf	Pertaining to the surface of the particle in the solid phase
	Pertaining to the average over the volume of a porous domain
s	*avg* Pertaining to the average over the volume of the solid particle
i	Pertaining to region i where $i \in \{0, 1, 2, 3, 4\}$
ij	Pertaining to the interface between regions i and j, where $i, j \in \{0, 1, 2, 3, 4\}$
i,ij	Pertaining to the interface between regions i and j on the side of region i where $i, j \in \{0, 1, 2, 3, 4\}$

Rigorous safety tests have been conducted on lithium-ion (Li-ion) batteries to establish safety standards for abnormal conditions like overcharge (OC), however over-discharge (OD) effects on batteries are often overlooked.[1–3] OD is the process of discharging a cell to a voltage level below the recommended manufacturer limit.[4] Over-discharge can be understood on the degree of de-lithiation from the anode i.e. by looking at the anode potential vs Li/Li$^+$. Slight or shallow over-discharge occurs when the cell voltage goes below the specified lower voltage limit, in this study that is 2.5 V. When this cell is discharged down from 2.5 V to 2 V, the anode potential ranges from 0.8 V–1 V vs Li/Li$^+$. If a cell is discharged further, to a terminal voltage of 1.5 V–1.8 V, we see the anode potential increase slightly to around 1.2 V–1.5 V vs Li/Li$^+$. Copper (Cu) dissolution from the anode current collector has been observed experimentally during such cases of shallow OD.[5] When cells are discharge below a terminal voltage of 1 V, we see the anode potential increase quickly above 1.5 V and when the terminal voltage is $<$0.0 V, and the anode potential increases above 3 V vs Li/Li$^+$, Cu dissolution from the anodic current collector can lead to severe capacity loss and the formation of copper bridges that internally short the cell.[6] Under subtle OD conditions, the dissolution of copper and its plating in the subsequent charge cycle can cause excess heat generation during cell cycling and has been found in some cases to lead to temperatures $>$150 °C.[7] The mechanism and rates for Cu dissolution and the resulting products formed Cu(OH)$_2$ and CuO are not well understood.[8–10]

On the other hand, OC occurs when a battery is charged beyond the upper voltage cutoff limit because the battery management system (BMS) fails to regulate the cell voltage, accumulating excess energy in the cell.[4] OC of Li-ion batteries accelerates degradation by inducing

---

[=] Equal Contribution.
[*] Electrochemical Society Member.
[**] Electrochemical Society Fellow.
[z] E-mail: venkat.subramanian@utexas.edu

lithium plating, which leads to a loss of the cyclable lithium, consumption of electrolyte, and a capacity imbalance between electrodes.[11,12] Both over-charging and over-discharging can lead to higher amounts of heat generation, stemming from an increase in cell polarization and impedance due to the accumulation of side reaction effects, thereby increasing the risk of thermal runaway.[11] Another aspect of off-nominal conditions is the extreme degree of (de) lithiation a cell's electrode is subjected to; the diffusion coefficient of lithium in electrode materials used in commercial Li-ion batteries have a non-linear response to the SoC and changes by an order of magnitude at extremely low values as is observed during OD.[13]

Empirical equivalent circuit impedance models[14] and fault detection and diagnosis models[15,16] have been considered for modeling OD in Li-ion batteries. However, there are very few examples in the literature of physics-based OD models. Our objective is to advance a physics-based modeling approach to understand the influence of OD on the thermal and electrochemical behavior of Li-ion batteries. Note that for modeling, we consider a battery to be composed of a single cathode, separator and electrode sandwich representing the full jelly roll construction of a Li-ion battery. The Tanks-in-Series (TiS) approach introduces volume averaging of the pseudo-two-dimensional (P2D) equations over distinct battery regions, namely, cathode, separator, and anode.[17] Further, the TiS model achieves reasonable agreement with the P2D model and demonstrates computational efficiency allowing for real-time applications of OC/OD monitoring.

The Thermal Tanks-in-series (TTiS)[18] battery model is a good candidate for predicting the changes in the battery's state-of-charge (SoC) and temperature, both being important variables in an OD model, which affects cell polarization and thermodynamics. The scope of this work is to develop a TTiS model with non-linear diffusivity[14] for slight OD conditions (till 1.5 V) and an approximate depth of discharge (DOD) $<$ 105% (DOD - capacity withdrawn/nominal cell capacity x 100).

Capacity fade occurs due to loss of lithium inventory, loss of active material, and increases in the internal resistance of the cell.[19] Various mechanisms have been studied and experimentally reported in the literature to cause these kinds of capacity fade depending on several factors such as the electrode material, electrolyte composition, operational voltage range, C-rate, operating environment, physical and chemical properties of the battery. The dominant mechanisms observed during a cell's normal operation are the formation of the solid electrolyte interphase (SEI) layer, lithium plating, cathode electrolyte interface (CEI) layer, and manganese (Mn) dissolution from Mn-containing cathodes.[20] During OD, as the anode open-circuit potential (OCV) rises above 1.5 V (vs Li/Li$^+$), copper from the anodic current collector strips and is deposited during the subsequent charging cycle onto the anode active material surface, cathode active material surface and can block the separator pores. The deposited copper forms a fresh surface for the growth of fresh SEI layer and is shown to cause accelerated SEI growth with subsequent cycling following an over-discharge cycle.[6] During severe OD, the exothermic breakdown of the SEI layer has been reported leading to elevated cell temperatures and risk of thermal runaway.[5]

The TTiS model is used to study the effect of various capacity fade mechanisms occurring during over-discharge under various over-discharge cycling protocols. The model simulation was used to study the temperature response and internal heat generation from various side reactions occurring under different protocols. The objective of this paper is to highlight the steps involved in simulating OD conditions, the effect of non-linear diffusivity on the cell behavior, and to characterize and understand the interplay of various capacity fade mechanisms occurring in a cell under various over-discharge cycling protocols.

Model Development

The TTiS battery model was proposed by Subramaniam et al.[18] It was derived by systematically volume-averaging each governing equation in the P2D model. The following approximations were considered while developing the TTiS model: (*a*) Approximating interfacial fluxes and determining interfacial values by imposing mass and charge conservation at the domain interfaces (for example, cathode-separator and separator-anode interface), and (*b*) using the electrode-averaged pore wall flux to estimate the electrode-averaged potential. For closure, the interfacial values in the TTiS model are derived using boundary conditions at the interfaces that establish the mass flow coupling between the cathode-separator-anode. The volume averaged TTiS model achieves excellent accuracy with respect to the P2D model for the cell parameters and operating conditions, taken in this work and as shown previously.[17] The volume averaging does cause certain limitations in discerning the effect of spatial heterogeneities in the electrode region, which become relevant for thick electrodes and high C-rate operation. In such cases the internal variables differ near the current collector and

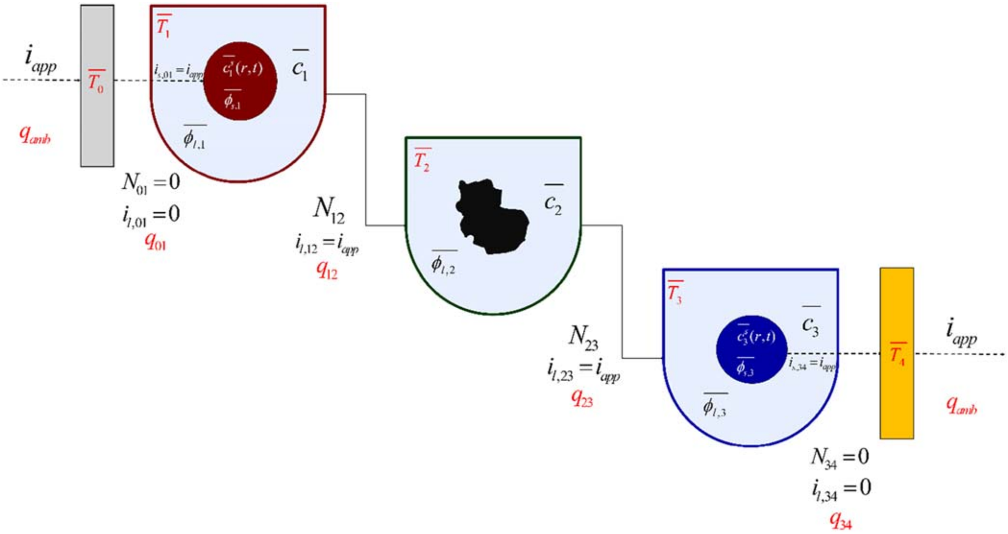

Figure 1. The extended Tanks-in-Series (TiS) model for thermal electrochemical model. Additional variables introduced due to the consideration of thermal effects are highlighted in red. In particular, the average temperature $\overline{T_i}$ is introduced in each "Tank" by way of the heat conservation equations. The volume-averaged form of the equations also includes the interfacial heat fluxes $\overline{q_{ij}}$. The cell as a whole exchanges heat with the ambient surroundings via the external heat flux q_{amb}.[13]

Table I. Governing equations of the Thermal Tanks-in-Series Model for the porous domains.

Equation	Positive Electrode (Region 1)	Separator (Region 2)	Negative Electrode (Region 3)
Electrolyte Mass balance	$\frac{d\overline{c_1}}{dt}=\frac{\frac{2D_e(c_{12},\,T_{12})(\overline{c_2}-\overline{c_1})}{\frac{l_1}{\varepsilon_1^{b_1}}+\frac{l_2}{\varepsilon_2^{b_2}}}}{\varepsilon_1 l_1}+(1-t_+^0)\frac{i_{app}}{F\varepsilon_1 l_1}$	$\frac{d\overline{c_2}}{dt}=\frac{\frac{-2D_e(c_{12},\,T_{12})(\overline{c_2}-\overline{c_1})}{\frac{l_1}{\varepsilon_1^{b_1}}+\frac{l_2}{\varepsilon_2^{b_2}}}+\frac{2D(c_{23},\,T_{23})(\overline{c_3}-\overline{c_2})}{\frac{l_2}{\varepsilon_2^{b_2}}+\frac{l_3}{\varepsilon_3^{b_3}}}}{\varepsilon_2 l_2}$	$\frac{d\overline{c_3}}{dt}=\frac{\frac{-2D_e(c_{23},\,T_{23})(\overline{c_3}-\overline{c_2})}{\frac{l_2}{\varepsilon_2^{b_2}}+\frac{l_3}{\varepsilon_3^{b_3}}}}{\varepsilon_3 l_3}-(1-t_+^0)\frac{i_{app}}{\varepsilon_3 l_3}$
Electrolyte Charge conservation	$i_{app}=-2\kappa(c_{12},\,T_{12})\left(\frac{\overline{\phi_{l,2}}-\overline{\phi_{l,1}}}{\frac{l_1}{\varepsilon_1^{b_1}}+\frac{l_2}{\varepsilon_2^{b_2}}}\right)$ $+\frac{4RT_{12}(1-t_+^0)}{F}\nu(c_{12},\,T_{12})\kappa(c_{12},\,T_{12})\frac{1}{c_{12}}\left(\frac{\overline{c_2}-\overline{c_1}}{\frac{l_1}{\varepsilon_1^{b_1}}+\frac{l_2}{\varepsilon_2^{b_2}}}\right)$	$\phi_{l,12}=\left(\frac{\frac{\varepsilon_1^{b_1}}{l_1}\overline{\phi_{l,1}}+\frac{\varepsilon_2^{b_2}}{l_2}\overline{\phi_{l,2}}}{\frac{\varepsilon_1^{b_1}}{l_1}+\frac{\varepsilon_2^{b_2}}{l_2}}\right)=0$	$i_{app}=-2\kappa(c_{23},\,T_{23})\left(\frac{\overline{\phi_{l,3}}-\overline{\phi_{l,2}}}{\frac{l_3}{\varepsilon_3^{b_3}}+\frac{l_2}{\varepsilon_2^{b_2}}}\right)+\frac{4RT_{23}(1-t_+^0)}{F}\nu(c_{23})\kappa(c_{23},\,T_{23})\frac{1}{c_{23}}\left(\frac{\overline{c_3}-\overline{c_2}}{\frac{l_2}{\varepsilon_2^{b_2}}+\frac{l_3}{\varepsilon_3^{b_3}}}\right)$
Energy balance equation	$\frac{d\overline{T_1}}{dt}=\frac{-\frac{2(\overline{T_1}-\overline{T_0})}{\frac{l_1}{\lambda_1}+\frac{l_0}{\lambda_0}}+\frac{2(\overline{T_2}-\overline{T_1})}{\frac{l_1}{\lambda_1}+\frac{l_2}{\lambda_2}}}{l_1}+\overline{Q_{rev,1}}+\overline{Q_{irrev,1}}+\overline{Q_{ohmic,1}}$	$\frac{d\overline{T_2}}{dt}=\frac{-\frac{2(\overline{T_2}-\overline{T_1})}{\frac{l_1}{\lambda_1}+\frac{l_2}{\lambda_2}}+\frac{2(\overline{T_3}-\overline{T_2})}{\frac{l_3}{\lambda_3}+\frac{l_2}{\lambda_2}}}{l_2}+\overline{Q_{ohmic,2}}$	$\frac{d\overline{T_3}}{dt}=\frac{-\frac{2(\overline{T_3}-\overline{T_2})}{\frac{l_2}{\lambda_2}+\frac{l_3}{\lambda_3}}+\frac{2(\overline{T_4}-\overline{T_3})}{\frac{l_4}{\lambda_4}+\frac{l_3}{\lambda_3}}}{l_3}+\overline{Q_{rev,3}}+\overline{Q_{irrev,3}}+\overline{Q_{ohmic,3}}$
Solid-phase mass conservation	$\frac{10}{7}\left(\frac{d\overline{c_1^{s,avg}}}{dt}\right)-\frac{3}{7}\left(\frac{d\overline{c_1^{s,surf}}}{dt}\right)=-15\overline{c_1^{s,avg}}+15\overline{c_1^{s,surf}}$ $-\frac{3}{7}\left(\frac{d\overline{c_1^{s,avg}}}{d\tau}\right)+\frac{3}{7}\left(\frac{d\overline{c_1^{s,surf}}}{d\tau}\right)=-3\frac{\overline{j_1}R_1}{D_1^s}+15\overline{c_1^{s,avg}}-15\overline{c_1^{s,surf}}$		$\frac{10}{7}\left(\frac{d\overline{c_3^{s,avg}}}{dt}\right)-\frac{3}{7}\left(\frac{d\overline{c_3^{s,surf}}}{dt}\right)=-15\overline{c_3^{s,avg}}+15\overline{c_3^{s,surf}}$ $-\frac{3}{7}\left(\frac{d\overline{c_3^{s,avg}}}{d\tau}\right)+\frac{3}{7}\left(\frac{d\overline{c_3^{s,surf}}}{d\tau}\right)=-3\frac{\overline{j_3}R_3}{D_3^s}+15\overline{c_3^{s,avg}}-15\overline{c_3^{s,surf}}$
Electrode charge conservation	$j_p=k_1(\overline{c_1})_1^{\alpha_{c,1}}(c_1^{s,\,\max}-\overline{c_1^{s,surf}})^{\alpha_{a,1}}(\overline{c_1^{s,surf}})^{\alpha_{c,1}}\left(\exp\left(\frac{\alpha_{a,1}F\overline{\eta_1}}{R\overline{T_1}}\right)-\exp\left(\frac{-\alpha_{c,1}F\overline{\eta_1}}{R\overline{T_1}}\right)\right)$ $\overline{\eta_1}=\overline{\phi_{s,1}}-\overline{\phi_{l,1}}-U(\overline{c_1^{s,surf}})$		$j_n=k_3(\overline{c_3})^{\alpha_{a,3}}(c_3^{s,\,\max}-\overline{c_3^{s,surf}})^{\alpha_{a,3}}(\overline{c_3^{s,surf}})^{\alpha_{c,3}}\left(\exp\left(\frac{\alpha_{a,3}F\overline{\eta_3}}{R\overline{T_3}}\right)-\exp\left(\frac{-\alpha_{c,3}F\overline{\eta_3}}{R\overline{T_3}}\right)\right)$ $\overline{\eta_3}=\overline{\phi_{s,3}}-\overline{\phi_{l,3}}-U(\overline{c_3^{s,surf}})$

Table II. Additional constitutive equations for the Thermal Tanks-in-Series models.

$$Q_{irrev,i} = Fa_i j_i [\phi_{s,i} - \phi_{l,i} - U(c_i^{s,surf})], \quad i \in \{1, 3\}$$

$$Q_{rev,i} = Fa_i j_i T_i \left[\frac{\partial U(c_i^{s,surf})}{\partial T} \right], \quad i \in \{1, 3\}$$

$$Q_{ohm,i} = \sigma_{eff,i} \left(\frac{1}{l_i} \frac{\partial \phi_{s,i}}{\partial x} \right)^2 + \left(\kappa_{eff,i} \left(\frac{1}{l_i} \frac{\partial \phi_{l,i}}{\partial x} \right) - \frac{2\kappa_{eff,i} R T_i}{F} (1 - t_+^0) \left(1 + \frac{\partial \ln f}{\partial \ln c_i} \right) \frac{1}{l_i^2} \frac{1}{c_i} \frac{\partial c_i}{\partial x} \right) \frac{\partial \phi_{l,i}}{\partial x}, \quad i \in \{1, 3\}$$

$$Q_{ohm,2} = \left(\kappa_{eff,2} \left(\frac{1}{l_2} \frac{\partial \phi_{l,2}}{\partial x} \right) - \frac{2\kappa_{eff,2} R T_2}{F} (1 - t_+^0) \left(1 + \frac{\partial \ln f}{\partial \ln c_2} \right) \frac{1}{l_2^2} \frac{1}{c_2} \frac{\partial c_2}{\partial x} \right) \frac{\partial \phi_{l,2}}{\partial x}$$

$$D_e(c_i, T_i) = 0.0001 \times 10^{-\left[4.43 + \frac{54}{T_i - 229 - 0.005 c_i}\right] - 0.00022 c_i}, \; i \in \{1, 2, 3\}$$

$$\kappa(c_i) = 1 \times 10^{-4} c_i \begin{bmatrix} (-10.5 + 0.0740 T_i - 6.96 \times 10^{-5} T_i^{\,2}) \\ + c_i (0.668 - 0.0178 T_i + 2.8 \times 10^{-5} T_i^{\,2}) \\ + c_i^2 (0.494 - 8.86 \times 10^{-4} T_i^{\,2}) \end{bmatrix}^2, \; i \in \{1, 2, 3\}$$

$$\left(1 + \frac{\partial \ln f}{\partial \ln c_i} \right) = \nu(c_i, T_i) = 0.601 - 7.5894 \times 10^{-3} \, c_i^{\,0.5} + 3.1053 \times 10^{-5} \, (2.5236 - 0.0052 \, T_i) c_i^{\,1.5}, \quad i \in \{1, 2, 3\}$$

$$U_i(T_i, \theta_i) = U_{i,ref}(T_{ref}, \theta_i) + (T_i - T_{ref}) \left[\frac{dU_i}{dT} \right] \Bigg|_{T_{ref}}, \; i \in \{1, 3\}$$

$$\frac{dU_1}{dT} = -0.001 \frac{\begin{bmatrix} 0.199521039 - 0.9283738822\theta_p + \\ 1.3645506890000003\theta_p^2 - 0.6115448939999998\theta_p^3 \end{bmatrix}}{\begin{bmatrix} 1 - 5.6614798869999997\theta_p + 11.476361191\theta_p^2 - \\ 9.8243121359999998\theta_p^3 + 3.0487550063\theta_p^4 \end{bmatrix}}$$

$$\frac{dU_3}{dT} = 0.001 \frac{\begin{bmatrix} 0.005269056 + 3.2992657709\theta_n - 91.79325799\theta_n^2 + \\ 1004.9110008\theta_n^3 - 5812.278127\theta_n^4 + 19329.7549\theta_n^5 - \\ 37147.8947\theta_n^6 - 38379.18127\theta_n^7 - 16515.05308\theta_n^8 \end{bmatrix}}{\begin{bmatrix} 1 - 48.092872227\theta_n + 1017.234804\theta_n^2 - \\ 10481.80419\theta_n^3 + 59431.3\theta_n^4 - 195881.6488\theta_n^5 + \\ 374577.3152\theta_n^6 - 385821.1607\theta_n^7 + 165705.8597\theta_n^8 \end{bmatrix}}$$

$$D_{i,eff}^s = D_i^s \exp\left(-\frac{E_a^{D_i^s}}{R} \left[\frac{1}{T_i} - \frac{1}{T_{ref}} \right] \right), \; i \in \{1, 3\}$$

the separator and representing this system with an averaged value will lead to inaccuracies in predictions. It is important to keep these limitations in mind when simulating the TTiS model. The pictorial representation of the TTiS model is shown in Fig. 1, and the detailed derivation can be found elsewhere.[2] In this work, the volume-averaged solid-phase concentrations solved in the radial direction are approximated using weak-form Galerkin approximation.[21] The final set of equations in the TTiS model used in this work are given in Table I, and the additional constitutive equations are summarized in Table II. The model solves for average electrolyte concentration in the cathode/separator/anode $\{\overline{c_1}, \overline{c_2}, \overline{c_3}\}$, average electrolyte potential in the cathode/separator/anode $\{\overline{\phi_{l,1}}, \overline{\phi_{l,2}}, \overline{\phi_{l,3}}\}$, average solid concentration in the cathode and anode $\{\overline{c_1^{s,avg}}, \overline{c_3^{s,avg}}\}$, solid particle surface concentration in the cathode and anode $\{\overline{c_1^{s,surf}}, \overline{c_3^{s,surf}}\}$, and average solid-phase potential in the cathode and anode $\{\overline{\phi_{s,1}}, \overline{\phi_{s,3}}\}$. Note that there are two averages: $\overline{c_1}$ represents the average concentration of lithium in the electrolyte for the cathode region and $\overline{c_1^{s,avg}}$ represents the average concentration inside a solid particle, averaged over the thickness of the cathode.

Experimental protocol and computational details.—To understand the key considerations in extending a battery model to perform OD simulation, a TTiS model was solved in MATLAB using the ode15i solver. Model derivation, equations, and expressions can be found in our previous work.[18]

For parametrization and experimental validation of the model, two 3.25 Ah NCR18650B cells, with an NCA cathode and a graphite anode, were first discharged down to 2.5 V (Cell 1) and 1.5 V (Cell 2), respectively. The two cells were then cycled at a C/2 CC charge step followed by a CV step until the current dropped to a value of C/50. Next, a 60 s rest step was performed, followed by a C/2 CC discharge step. Finally, a 60 s rest step was conducted, completing the protocol, for two different voltage ranges; Cell 1 for the normal discharge (ND) range of 4.2 V–2.5 V and Cell 2 for an over-discharge (OD) condition of 4.2 V–1.5 V. Voltage and temperature data were collected for these cells and used for the model parametrization and validation. A single thermocouple was placed on the surface of the cell, near the cap (i.e. positive electrode) of the cylindrical cell.

To understand the capacity fade behavior experimentally, cell cycling experiments were conducted using three different cycling protocols at Purdue University.[7] The first cycling protocol, labeled as normal discharge (ND) cycling, involves charge-discharge steps based on the above-detailed procedure, within the normal discharge voltage range of 4.2 V–2.5 V. It is called normal discharge, as the cycling procedure is done in accordance with manufacturer recommendations. The second protocol labeled as over-discharge (OD) cycling, involves 5 cycles of OD down to 1.5 V followed by ND voltage window cycling, and the final protocol, labeled Periodic Over-Discharge (POD) cycling, is 5 cycles of OD down to 1 V, followed by 20 cycles of ND voltage window cycling repeating periodically. All experimental cycling is done until 20% capacity fade is reached based on the initial cycle's capacity. These experimental cycling protocols were chosen to study the impact of slight over-discharge, for a few cycles at the start and for a periodic over-discharge scenario. Our aim is to develop a model with relevant capacity fade mechanisms to capture the effect of these protocols on a cell to understand the initiation and propagation of certain mechanisms (i.e. copper dissolution) under long term cycling. Extreme over-discharge and abuse conditions are highly relevant cases to analyze, however since they lead to immediate cell failure, a long-term cycling study cannot be performed with these cases. We will look to expand on this work with failure tests in a future study. A schematic representing the experimental data collected is shown in Fig. 2.

Results and Discussion

To use the TTiS model for understanding over-discharge cycling, we first need to identify the correct parameters for the model that satisfy the first cycle voltage vs time curves. The model is parametrized using two voltage windows, the ND voltage vs time curve, giving one parameter set (Set 1), and the second parameter set (Set II) uses both the ND & OD voltage vs time curves for parametrization. Then the model is simulated under 3 different cycling protocols to compare against experimental data, namely the ND, OD, and POD cycling cases. The agreement of the final simulations with experimental data are quantified by calculating the RMSE error and is reported in their respective figures. Finally, a case study evaluates the effect of C-rate and ambient temperature on capacity fade characteristics of the cell. The simulations performed are summarized in Fig. 2. We will now look at each of these simulations in detail.

Parametrization: 1st cycle voltage vs time simulation.—The primary objective of any battery model is to reasonably predict the voltage-time behavior of an electrochemical cell under various operating conditions. A base set of cell parameters and OCV curves were obtained from the literature[22] and used for simulations. A key modification to the model equations involves the addition of concentration-dependent diffusivity to the solid phase.[21] The motivation to include variable diffusivity is the non-linear dependence of lithium diffusion in electrode materials to the its degree of (de) lithiation, especially at lower concentrations as seen during OD.[13]

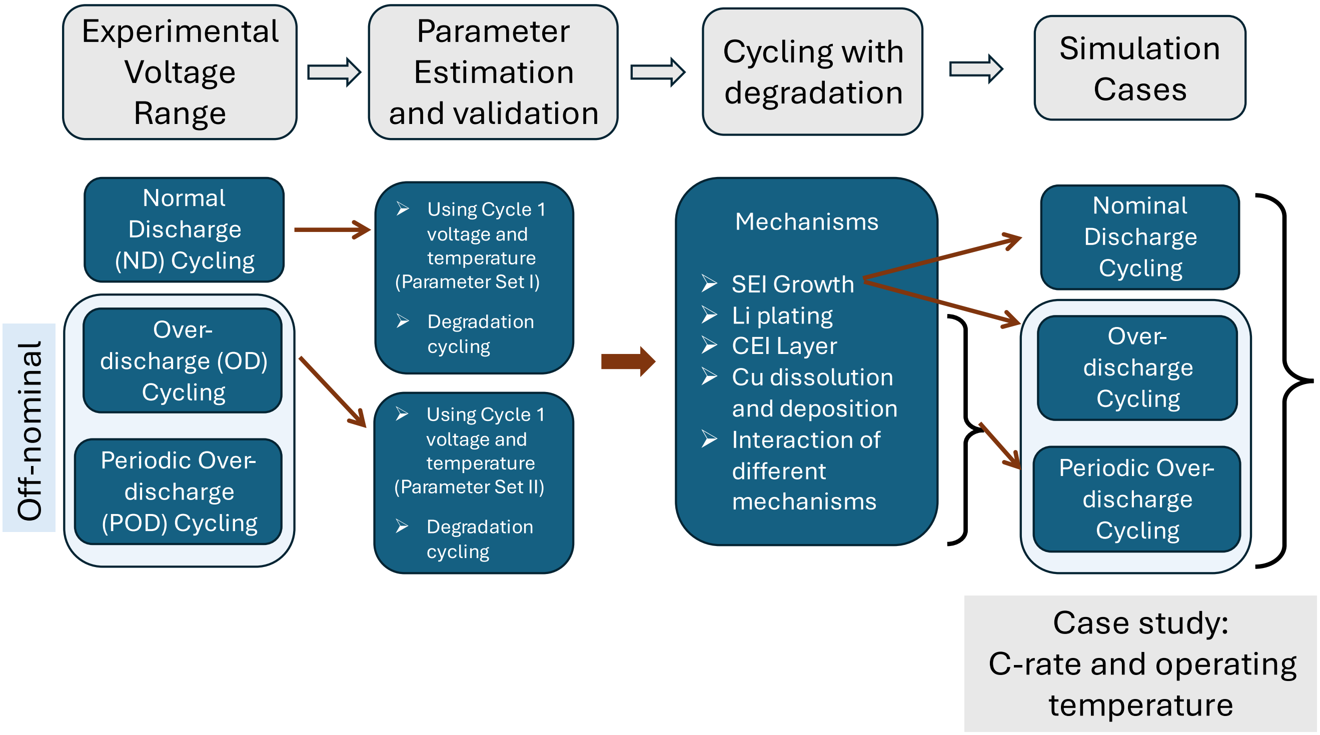

Figure 2. Schematic for experimental data collected and model simulations done. The model is parametrized for two parameter sets, Set I, using cycle 1 voltage vs time of the normal discharge case and Set II using cycle 1 voltage vs time of both the normal discharge and over-discharge cycle.

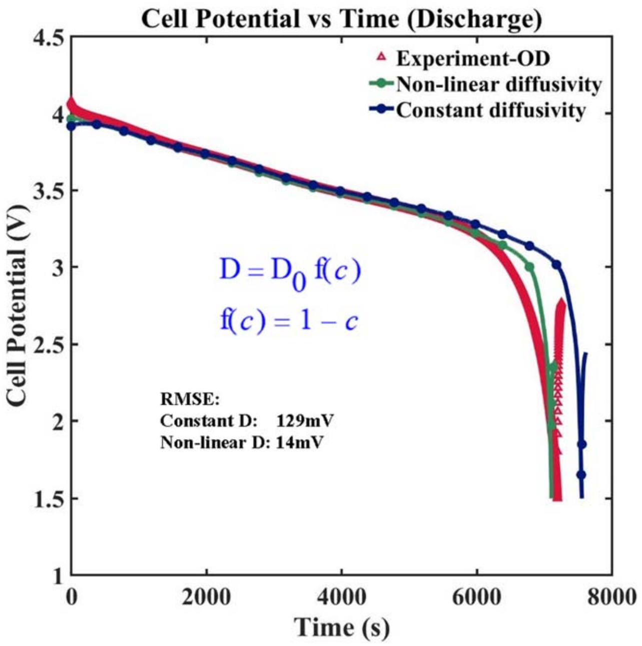

Figure 3. Addition of non-linear diffusion to the model vs using constant diffusivity, shows a better voltage vs time fit for the OD case, while using the same SoC values as in the ND case.

Figure 3, shows the model result vs ND voltage-time curve with and without varying diffusivity. The variable diffusivity is included in all the model simulations henceforth.

The final set of parameters, listed in Table III, were tuned from literature values to match the charge and discharge voltage-time behavior for the ND voltage range as seen in Set I of Figs. 4a and 4b. We see a good agreement between Set I model simulation and the voltage-time data.

Next, the Set I parameter set was used to simulate the model to perform charge and over-discharge down to 1.5 V, as seen in Figs. 4c and 4d. In Fig. 4d, the model discharge voltage stops at 1.7 V and starts increasing before the cut-off voltage of 1.5 V is hit, the model fails to simulate further as the concentration of lithium in the anode approaches 0 and the OCV expression gives meaningless results. Hence the model was re-parametrized using the first cycle voltage vs time data of both the ND and OD voltage range, giving us the Set II parameter set. The simulations were able to predict the OD case, as the OCV functions for the cathode and anode were chosen such that the Li concentration in the electrode, during simulation falls within meaningful values when going to these extreme voltages. The final concentration of Li in the anode and the cathode depends on the initial values chosen as well as the capacity utilization during cycling simulation. Redefining these initial values for both the anode and the cathode allows the cell to operate in a meaningful concentration window during cycling, thereby preventing unrealistic values seen at the end of discharge. Figures 4c and 4d shows simulation results using Set II parameters, which not only match the voltage-time curve for OD but also for the ND voltage regime as seen in Figs. 4a and 4b.

Once the voltage-time curves were simulated and found to be in agreement with the data, the thermal model parameters were tuned to match the experimentally measured cell temperatures as shown in Figs. 5c and 5d. This involved identifying the key heat generation term during discharge and charge, as seen in Figs 5a and 5b respectively, and tuning the expression for the entropic heating term ($Q_{rev,i}$) as it is the most volatile and significant contributor to heat generation in the cell. The agreement achieved for the voltage-time as well as temperature-time curves, for the ND and OD voltage protocol highlights the fidelity of the model developed to simulate different discharge protocols and conditions.

Parameter values used in the TTiS model are listed in Table III. We arrived at a set of parameters and initial conditions for our model

Table III. Model parameters.[17]

Parameter	Cathode	Separator	Anode
$C_{i,\,max}$ Maximum particle phase concentration (mol/m^3)	50488		31667
C_0 Initial electrolyte concentration (mol/m^3)	—	1000	—
l_i Electrode Thickness (m)	7.25×10^{-5}	0.20×10^{-4}	7.35×10^{-5}
R_i Characteristic Particle Radius (m)	4.55×10^{-6}	—	7.70×10^{-6}
ε_i Porosity in positive electrode	0.24	0.40	0.26
ε_{fi} Filler fraction[a)]	0.02	—	0.02
b_i Bruggeman tortuosity correction	1.5	1.5	1.5
α_a electrode reaction anodic coefficient	0.5	—	0.5
α_c electrode reaction cathodic coefficient	0.5	—	0.5
D_i^s Solid Phase Diffusivity (m^2/s)[a)]	0.5×10^{-13}	—	0.7×10^{-13}
Ea_D Activation energy for temperature dependent solid phase diffusion (J/mol)	5000	—	5000
Ea_k Activation energy for temperature dependent kinetic rate constant (J/mol)	5000	—	5000
C_p Specific heat	700	700	700
λ_i Thermal Conductivity (W / (m K))	2.1	0.16	1.7
ρ_i Density (kg/m^3)	2500	1100	2500
θ_i State of charge[a)]	Set I 0.92	—	Set I 0.021
	Set II 0.99	—	Set II 0.20
k_i Electrode reaction rate constant (m$^{2.5}$/(mol$^{0.5}$s)	1.43×10^{-11}	—	2.88×10^{-12}
Q_{cell} Capacity of cell (Ah)	3.25		
A_{cell} Cross-sectional area of electrode (m^2)	0.081		
t_1 Li ion transference number	0.38		
Kr Contact resistance in the circuit (Ohm)	0.255×10^{-3}		
F Faraday's constant (C/mol)	96487		
R Gas Constant J/(mol K)	8.314		
T_{amb} Ambient Temperature (K)	294.65		
T_{ref} Reference Temperature (K)	298.15		
h_{amb} Ambient heat transfer coefficient (W/(m^2 K))[a)]	2		
Rate test C-rate (1/h)	0.5		
Expression used in the entropic heat generation term[a)]	Set I	$\frac{dU_1}{dT} = -0.001\frac{\begin{bmatrix}0.199 - 0.928\theta_p + \\ 1.36\theta_p^2 - 0.611\theta_p^3\end{bmatrix}}{\begin{bmatrix}1 - 5.66\theta_p + 11.47\theta_p^2 - \\ 9.82\theta_p^3 + 3.05\theta_p^4\end{bmatrix}}$	$\frac{dU_3}{dT} = 0.001\frac{\begin{bmatrix}0.00527 + 3.299\theta_n - 91.793\theta_n^2 + \\ 1004.911\theta_n^3 - 5812.278\theta_n^4\end{bmatrix}}{\begin{bmatrix}1 - 48.09228\theta_n + 1017.234\theta_n^2 - \\ 10481.804\theta_n^3 + 59431.343\theta_n^4\end{bmatrix}}$
	Set II	$\frac{dU_1}{dT} = -0.001\frac{\begin{bmatrix}0.351 - 0.875\theta_p + \\ 1.845\theta_p^2 - 0.784\theta_p^3\end{bmatrix}}{\begin{bmatrix}1 - 9.25\theta_p + 9.45\theta_p^2 - \\ 7.23\theta_p^3 + 5.34\theta_p^4\end{bmatrix}}$	$\frac{dU_3}{dT} = 0.001\frac{\begin{bmatrix}0.006214 + 2.5638\theta_n - 103.241\theta_n^2 + \\ 1402.123\theta_n^3 - 4140.237\theta_n^4\end{bmatrix}}{\begin{bmatrix}1 - 47.142\theta_n - 7139.235\theta_n^2 + \\ 18243.12\theta_n^3 - 54981.283\theta_n^4\end{bmatrix}}$

a) parametric fit.

that agrees with experimental data. Several parameters were obtained from literature[22] and some were fitted (shown by * in Table III). The converged set of parameters and the MATLAB codes are shared as open-access codes for non-commercial purposes.

Capacity fade mechanisms.—The first cycle simulation is shown to match with experimental data, and we will now discuss the addition of capacity fade mechanisms involved in the cycling protocols under consideration. A list of mechanisms used is summarized in Table IV.

The addition of capacity fade mechanisms to battery models depends on factors such as the electrode material, electrolyte composition, operational voltage range and C-rate, which determines the type and amount of each mechanism that causes fade. The SEI layer is a major reason for the loss of cyclable lithium ions throughout a cell's operational lifetime, occurring at slow rates and room temperature conditions. During over-discharge, copper from the anodic current collector strips, and is deposited during the subsequent charging cycle onto the anode active material surface. The deposited copper forms a fresh surface for the growth of new SEI layer and is shown to cause accelerated SEI growth with subsequent cycling following an over-discharge cycle. During severe over-discharge, the exothermic breakdown of the SEI layer has been reported leading to elevated cell temperatures and risk of thermal runaway. The mechanism was modeled on experimental observations and characterization of over-discharge where plated copper was found on the electrode and separator surfaces, for cells being discharged to a terminal voltage of 1.5 V. For the chosen cycling

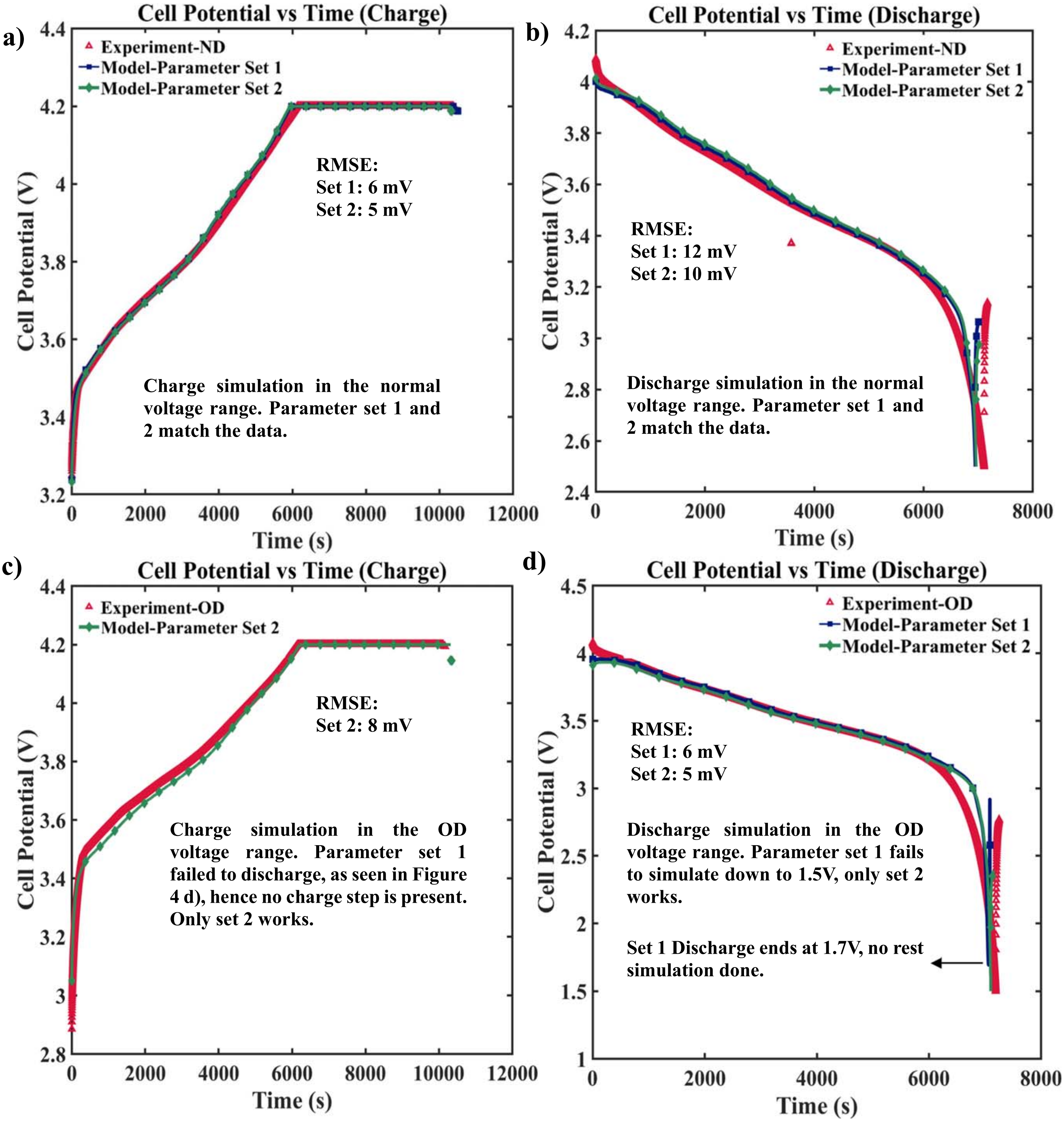

Figure 4. Voltage vs time plots using two parameter sets as Set I and Set II, i.e. parameter set I and parameter set II, for the normal discharge (ND) 2.5V–4.2 V (a) charge and (b) discharge plots and the over-discharge (OD) 1.5 V–4.2 V (c) charge and (d) discharge plots.

protocols in this study, which involves a shallow over-discharge, we have estimated the reaction potential and SoC window of operation to reflect the initiation of the Cu mechanisms only during over-discharge. The effect of a deeper depth of over-discharge and temperature on the mechanism will be studied in detail separately in future work. The choice of capacity fade mechanisms to be included in the electrochemical model was based on literature review and as per the operating C-rate and ambient temperature of the cell. Thus, the final set of fade mechanisms incorporated are i) solid-electrolyte interphase (SEI) layer growth, ii) Lithium plating, iii) cathode-electrolyte interphase, (CEI) layer growth, and iv) copper dissolution and deposition, which is observed during OD specifically. The variation in the conductivity of the SEI layer is also modeled due to copper deposition on the existing SEI surface.

Capacity fade cycling studies.— *SEI layer growth in: ND, OD and POD cycling.*—The effect of capacity fade is introduced for a cycling simulation in the ND voltage range, termed normal discharge cycling, and validated against experimental data. The cell was cycled until 20% capacity fade was recorded with respect to the initial cycle capacity.

Initially, only the diffusion-limited SEI layer mechanism was added to predict the capacity fade data as shown in Fig. 6a, highlighting the discharge capacity with every cycle. Adding only

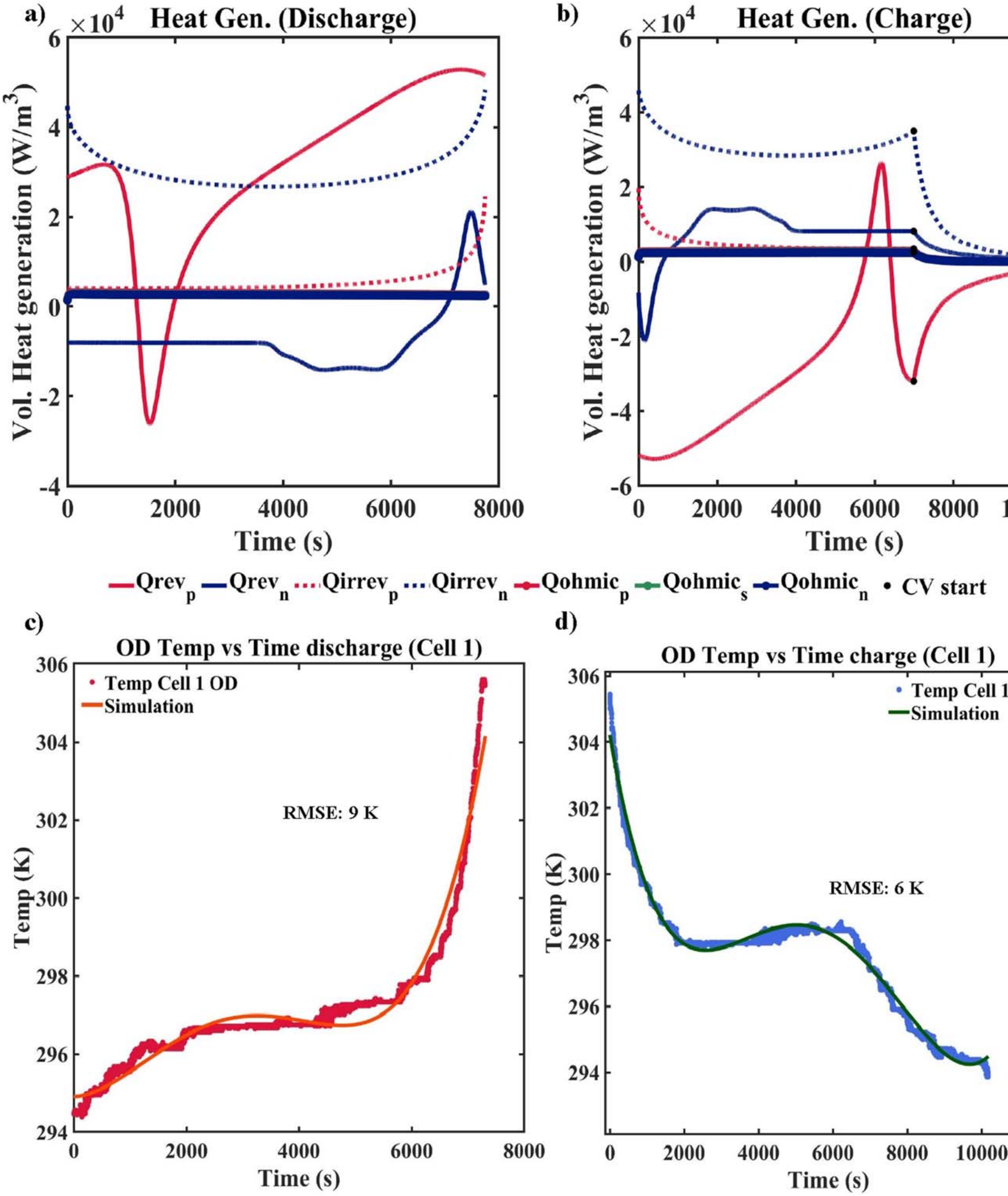

Figure 5. Internal heat generation rates for (a) discharge and (b) charge in the OD voltage window, showing that Q_{rev} (entropic heating) has the highest contribution. First OD cycle temperature vs time plots during (c) discharge and (d) charge.

the SEI layer growth we observe a good agreement between the experimental data and simulation results for the normal discharge case, and the current model reasonably captures the initial non-linear trend of capacity degradation attributed to the diffusion-limited SEI growth regime. Applying the same mechanism to the OD cycling case, a cycling simulation with 5 initial cycles of OD down to 1.5 V followed by the ND voltage range until 20% capacity fade, we observe that the initial 5 cycles have a higher capacity as seen in Fig. 6b. The cell being over-discharged to 1.5 V as opposed to 2.5 V contributes to the increased capacity output of the cell. Overall, the model can capture the experimental capacity data, highlighting that this protocol is quite similar to the normal discharge cycling case, meaning a few cycles of slight over-discharge to 1.5 V initially do not significantly affect the cell performance and behavior with continued ND voltage range cycling.

Figure 6c shows the discharge capacity vs cycle number for the POD cycling simulation with the SEI layer mechanism. Using the same SEI reaction parameter values as the previous two cases (ND

Table IV. Capacity fade mechanisms for the Tanks-in-Series model.

Mechanism	Equation
Solid Electrolyte Interface[15]	$\frac{d\delta_{sei}}{dt} = \frac{j_{sei}M_{sei}}{\rho_{sei}} + \frac{j_{pl}M_{Li}}{\rho_{Li}}$
	$j_{sei} = -k_{sei}(\overline{c_3^{s,surf}})^{\alpha_{c,3}} \exp\left(-\frac{E_a^{k_{sei}}}{R}\left[\frac{1}{T_3} - \frac{1}{T_{ref}}\right]\right)\left(\exp\left(\frac{-\alpha_{sei,3}F\overline{\eta_{sei}}}{R\overline{T_3}}\right)\exp(-\lambda_{sei}\delta_{sei})\right)$
Cathode Electrolyte Interface[16]	$\frac{d\delta_{cei}}{dt} = \frac{j_{cei}M_{cei}}{\rho_{cei}}$
	$j_{cei} = -k_{cei}(\overline{c_1^{s,surf}})^{\alpha_{a,3}} \exp\left(-\frac{E_a^{k_{cei}}}{R}\left[\frac{1}{T_1} - \frac{1}{T_{ref}}\right]\right)\left(\exp\left(\frac{-\alpha_{cei,1}F\overline{\eta_{cei}}}{R\overline{T_1}}\right)\exp(-\lambda_{cei}\delta_{cei})\right)$
Lithium Plating[16]	$j_{pl} = \frac{-i_{0\_pl}\left(\exp\left(\frac{-\alpha_{pl,3}F\overline{\eta_{pl}}}{R\overline{T_3}}\right)\right)}{\mathrm{F}}$
Copper Deposition and dissolution	$j_{Cu} = \frac{-i_{0\_Cu}\left(\exp\left(\frac{-\alpha_{Cu,3}F\overline{\eta_{Cu}}}{R\overline{T_3}}\right)\right)}{\mathrm{F}}$
	$\frac{d\varepsilon_{neg}}{dt} = \beta_{Cu}j_{Cu}F$
Change in SEI Conductivity	$\frac{d\kappa_{sei}}{dt} = -k_{0\_cu}i_{0\_Cu}$
Anode Flux balance	$j_n = j_{n\ \mathrm{int}} + j_{sei} + j_{pl} + j_{Cu}$
Cathode Flux balance	$j_p = j_{p\ \mathrm{int}} + j_{cei}$

and OD) we see the model predicts the capacity trend for the first 5 OD cycles and next 20 ND window cycles, then begins to over-predict the ND window capacity data with subsequent cycling. The difference between experimental and simulated capacity indicates the additional source of capacity loss when OD cycles are more frequent.

Multiple capacity fade mechanisms in POD cycling.—We have established that SEI growth alone cannot account for the losses to a cell undergoing POD cycling. The model overpredicts the experimental capacity with aging, requiring additional fade mechanisms to be included.

Along with the SEI layer formation, we consider the growth of the CEI layer as well as the loss of lithium inventory via reversible lithium plating. Figure 7a shows the simulated discharge capacity with three fade mechanisms vs experimental data for POD cycling. This simulation can be viewed in two parts, the capacity observed during the OD step and the capacity obtained during the ND window step. Three mechanisms show a higher overall fade, seen in the ND window capacity, as some lithium inventory is now lost in CEI layer formation and Li plating in addition to the SEI layer. However, the model still overpredicts the discharge capacity in this region. The capacity obtained during OD, is still higher than the experimentally observed capacity. This is possibly due to the reversible Li plating, which acts as a source of lithium when the cell is being forced to over-discharge, and due to Li plating not contributing to internal cell polarization unlike SEI and CEI layer growth. Lithium plating is observed in cells when the anode voltage drops below 0 V vs Li/Li$^+$, this has been widely studied and is the potential value we are using to initiate Li plating. In the first few cycles, Li plating is not observed as the anode over-potential does not drop below the required potential to favor this side reaction, which is typically seen when a fresh cell is charged above the 4.2 V upper voltage limit. However, as the cell ages, due to SEI and CEI layer formation as well as copper dissolution and deposition during over-discharge, the internal polarization increases for the cell and there is a loss in Li inventory. Additionally, the deposited copper causes a reduction in accessible active material, which in turn increases the current density across the anode. The increased polarization, loss of Li inventory and reduction of available active material all cause the aged cell's anode potential to drop below the 0 V threshold and initiate the plating reaction. Highly polarized cells will reach the lower terminal voltage limit with a short discharge time, attributing some capacity fade during the charge step to plating, allows for the cell to operate for a longer window with respect to voltage during each over-discharge step down to 1.5 V. This can explain the increasing gap between OD capacity and ND window capacity.

Finally, we add another key mechanism that activates only during OD and is a non-polarizing type of fade, copper dissolution. Figure 7b shows the results for this case, where we see a marked drop in capacity after each OD step. Cu dissolved during OD can deposit on the active material of the anode, cathode and block the porous separator as well. In this study, we have accounted for these effects of deposition by changing the active material fraction of the anode as Cu dissolution occurs (equations summarized in Table IV). Figure 7b still shows the model overpredicting, albeit slightly, the actual data during the ND operating window.

Finally, another effect of Cu deposition is the increased tendency of SEI formation in subsequent charging cycles, as there is a new non-insulating surface for the lithium and electrolyte to react. Linking Cu deposition to increased SEI formation in the model is accounted for by changing the effective conductivity of the SEI layer (κ_{sei}). Increasing the SEI conductivity, reduces the overpotential for SEI formation and increases the voltage window in which SEI can form during charging. Figure 7d includes the SEI linked Cu dissolution mechanism, CEI formation, Li plating and Cu dissolution, where we see the model predict both the OD capacity and the ND window capacity. The increasing gap between the over-discharge capacity and the ND window capacity is primarily due to two mechanisms, copper dissolution and deposition and the subsequent increased SEI layer formation after every 5 cycles of over-discharge. The deposited copper provides a new surface with a lower overpotential, due to the increased conductivity of the SEI layer, which causes increased SEI formation during subsequent steps. This result has also been experimentally observed.

Effect of C-rate and ambient temperature.—The mechanisms and the extent of degradation in Li-ion batteries are dependent on the

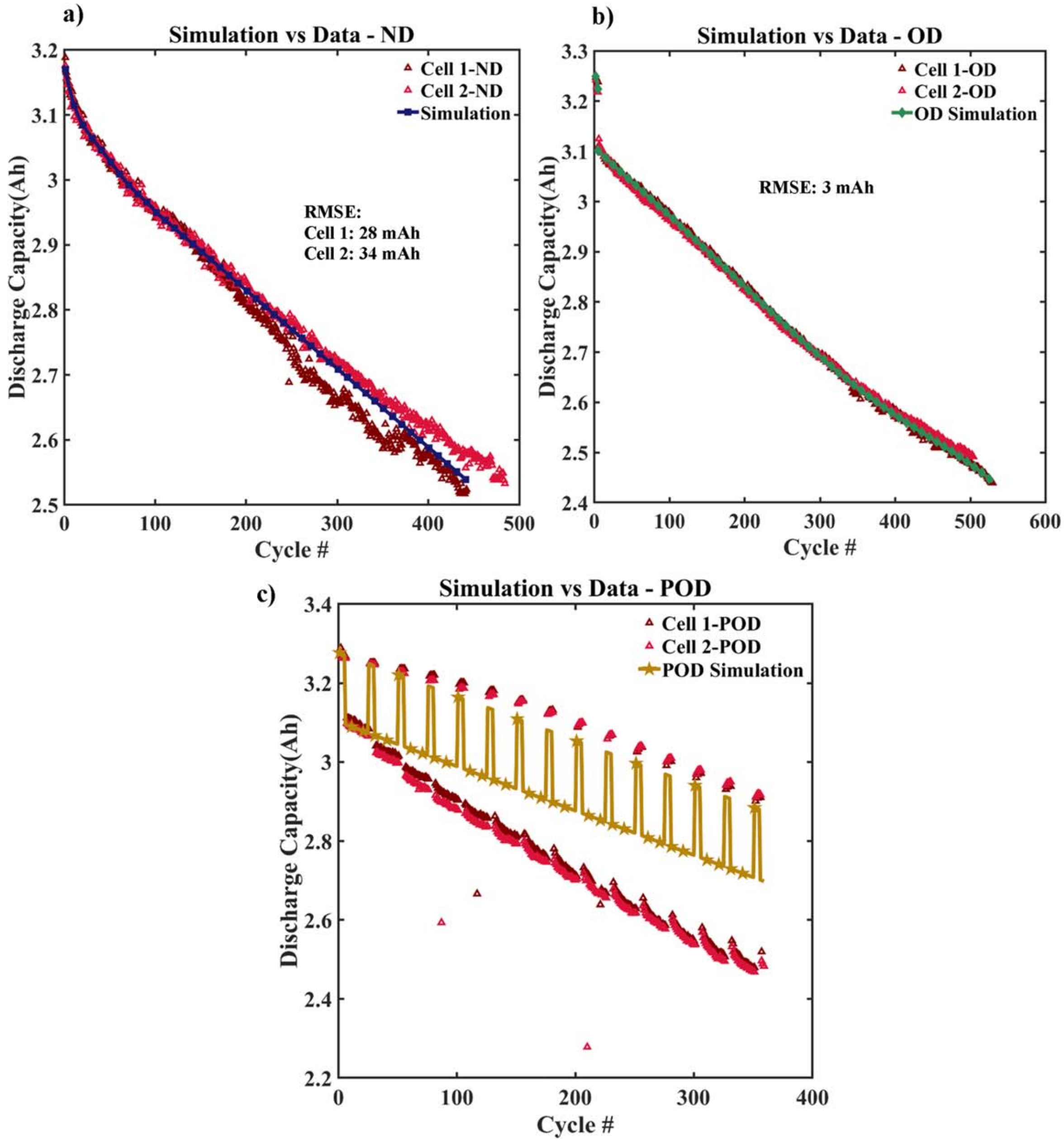

Figure 6. Discharge capacity with cycles, model vs data plot for (a) normal discharge (b) Over-discharge and (c) Periodic over-discharge using only SEI layer capacity fade.

cell chemistry, operation conditions, cycling protocol, and ambient temperature. We analyze the effect of C-rate and ambient temperature on the periodic over-discharge protocol as studied above. The baseline cycling protocol is a C/2 CC charge to 4.2 V, followed by a CV charge until the current drops to C/50. A C/2 CC discharge is then performed to 2.5 V for the normal regime and 1.5 V for the over-discharge cycles, all simulated at 25 °C. This protocol is followed for 5 cycles of over-discharge followed by 20 cycles of normal discharge till 20% of the initial capacity is reached. The same protocol is studied for the following cases, as seen in Fig. 8:

i) C/4 rate
This is a lower rate compared to the ND case and the simulation plots are shown in Fig. 8a. We observe that the initial capacity is higher, this is due to lower polarization occurring at the lower C-rate leading to a higher initial capacity. As cycling continues, we can observe the discharge capacity in two sections, one for the over-discharge capacity and the other for the normal regime discharge capacity. The normal regime capacity is consistently higher than the ND case as is evident with increasing cycle number. There is less overall fade at the lower C-rate due to lower SEI formation, lower CEI formation and lesser plating and copper dissolution. The contribution of individual mechanisms is evident in Fig. 8c, showing the simulated values of capacity lost due to each mechanism. The over-discharge capacity value is very similar to the baseline case as under both circumstances, the copper dissolution mechanism does not contribute significantly enough in the operating window to reduce the capacity when going to the 1.5 V cutoff.During CC discharge the temperature of a cell peaks just before reaching the cutoff voltage. Figure 9a shows the peak discharge temperature during C/2 POD cycling simulation vs experimental data. We see that although peak temperatures increase with cycles, the slope for OD peak temperature is higher than for ND window cycling, for the experimental data and simulation. For a lower C-rate we

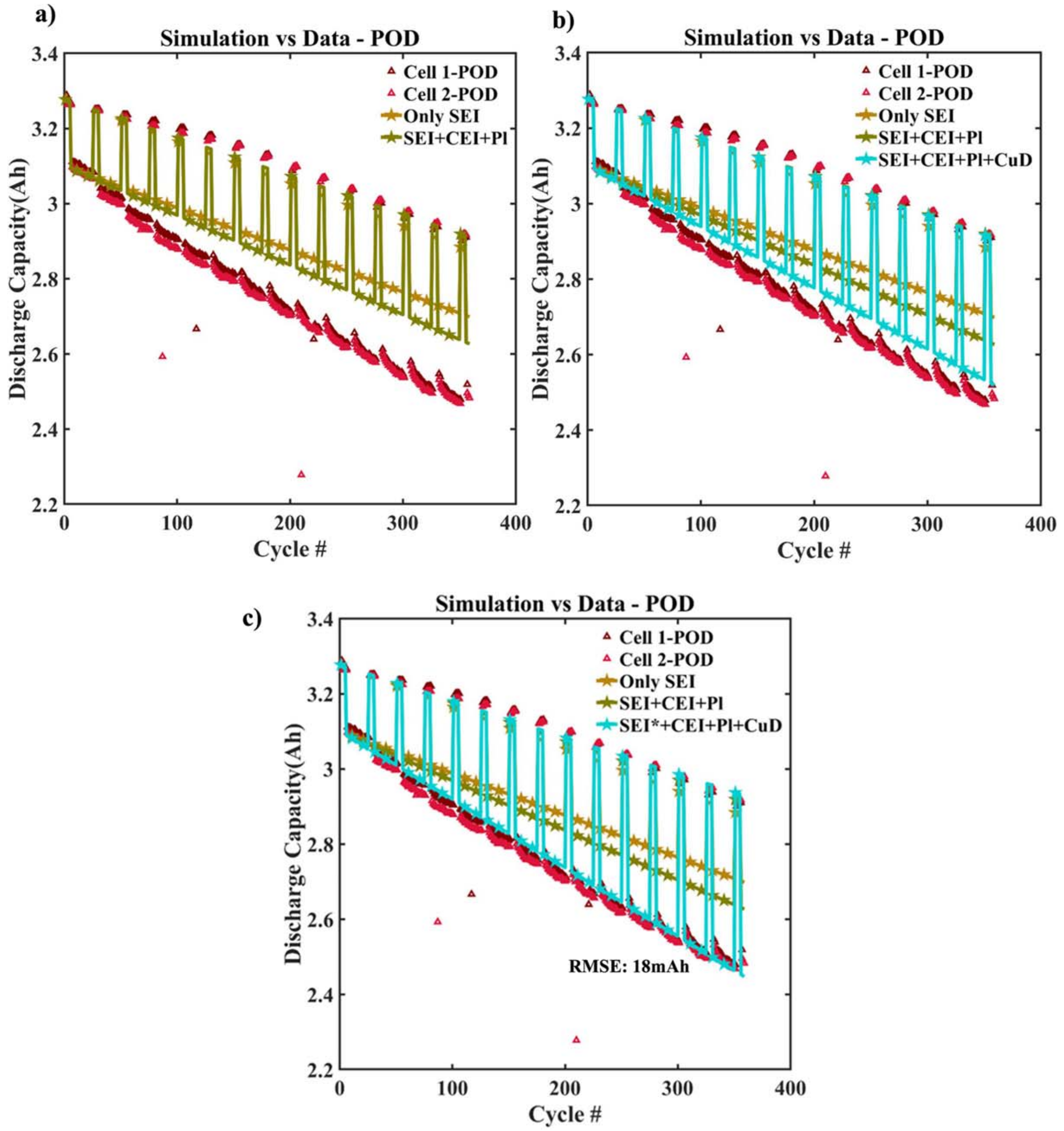

Figure 7. Multi-mechanism POD cycling including (a) SEI, CEI and Li plating (b) SEI, CEI, Li plating and, Cu dissolution (c) SEI coupled with Cu dissolution, CEI, Li plating and, Cu dissolution.

observe a similar effect, but with the difference between OD and ND window peak temperature being different based on the C-rate.

ii) 1 C rate

This is a higher rate compared to the baseline case, and the simulation plots are shown in Fig. 8a. We observe that the initial capacity is lower, this is due to higher polarization occurring at the higher C-rate leading to a lower initial capacity. As cycling continues, we can observe the discharge capacity in two sections, as observed in the previous case. The normal regime capacity is consistently lower than the baseline case as is evident with increasing cycle number. There is more overall fade at the higher C-rate primarily due to higher SEI formation, CEI formation and to a lesser extent Li plating and copper dissolution at this C-rate. The contribution of individual mechanisms is evident in Fig. 8c, showing the simulated values of capacity lost in each mechanism. The over-discharge capacity value is lower compared to the baseline case as the Cu dissolution mechanism and Li plating are triggered as the overpotential in the anode promotes this side reaction for a longer time as compared to the lower C-rates. Figure 8c highlights the increase in individual mechanisms, showing the highest percentage change of fade coming from the Li plating. The compounding effect of loss of capacity from the over-discharge regime and the normal regime, causes the capacity fade at a much higher rate compared to going from the C/4 to C/2 condition. The ambient temperature effect is analyzed in the section below.

iii) 15 °C

At a lower temperature, polarization is higher due to slower kinetics, diffusion, and conductivities. Figure 8b shows the simulation capacity vs cycles for various ambient temperatures. The lower temperature at 15 °C shows a lower initial capacity due to higher polarizations within the cell, causing the voltage cutoff to reach earlier. However, with cycling we observe that the three temperatures under study, meet at around 150 cycles

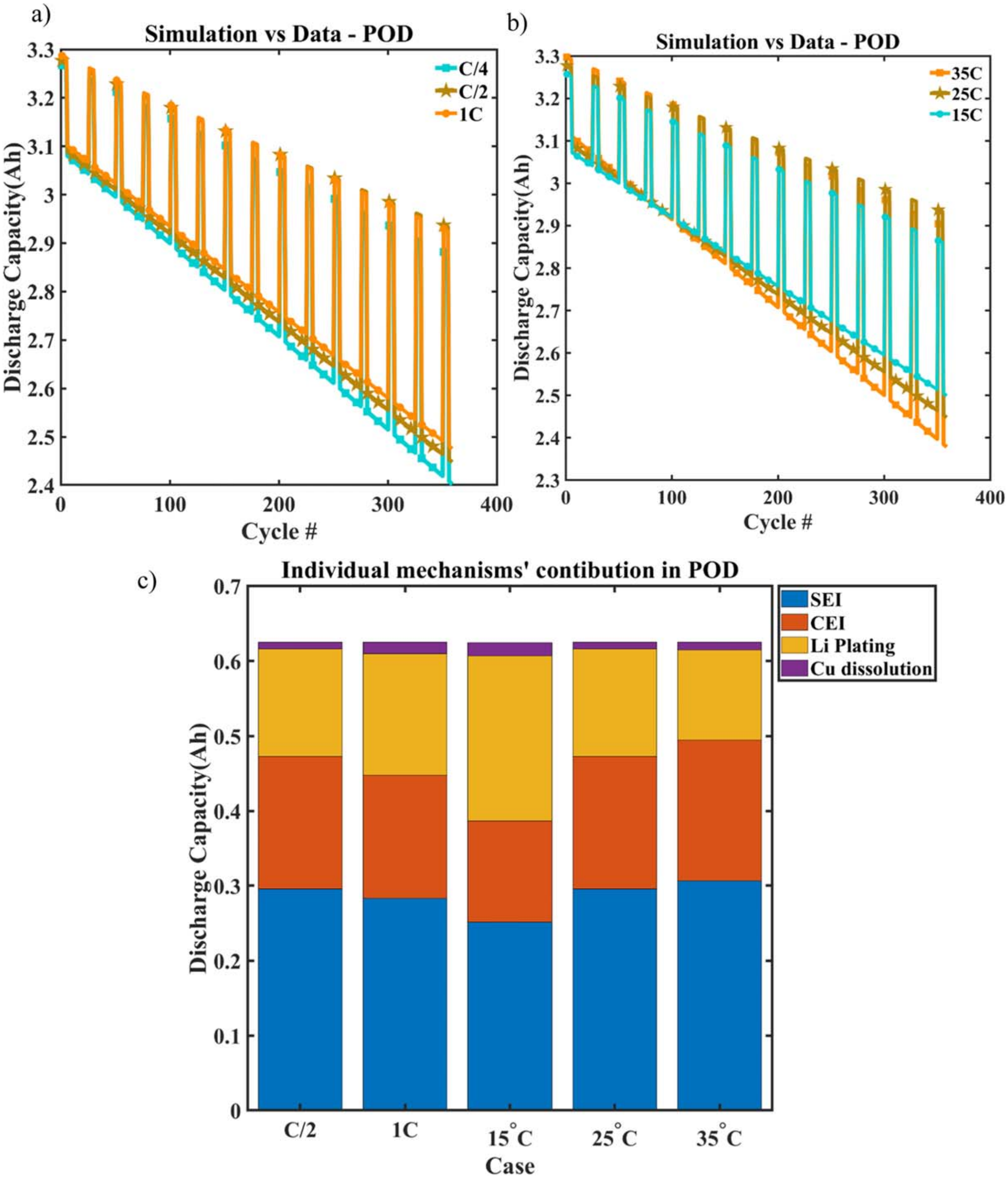

Figure 8. Capacity vs cycle number simulation for POD (a) under different C-rates (b) for different ambient temperatures. Individual mechanisms' contribution at 20% fade (c) under different C-rates and ambient temperatures.

and crossover, where the 15 °C case shows a higher capacity as compared to the baseline temperature case of 25 °C. With cycling, the amount of overall capacity fade for the 15 °C case, is lower leading to more available Li inventory during operation, the primary reason being the slower kinetics for SEI and CEI formation as seen in Fig. 8d. We can also see that the amount of copper dissolution and Li plating have increased as compared to the baseline case causing the OD capacity to fall well below the baseline values, over-discharging cold cells limits the incremental capacity highly as the high overpotentials cause side reactions to occur and force the cell to reach the 1.5 V cutoff faster. The cell operates differently in the two given conditions, i.e. the normal discharge and over-discharge voltage window, as compared to the baseline temperature case of 25 °C, showing a higher capacity in the normal voltage regime and a lower capacity when being over-discharged.

iv) 35 °C

At a higher temperature the low polarization is observed initially due to faster kinetics, diffusion, and conductivities. Figure 8b shows the simulation capacity vs cycles for various ambient temperatures. The higher temperature at 35 °C shows a higher initial capacity due to lower polarizations within the cell causing a higher initial discharge capacity to be achieved. After around 150 cycles however, we see the 35 °C case shows a lower capacity as compared to the baseline temperature case of 25 °C. With cycling, the amount of overall capacity fade for this case is much higher, leading to lesser available Li inventory during operation, the primary reason being the higher

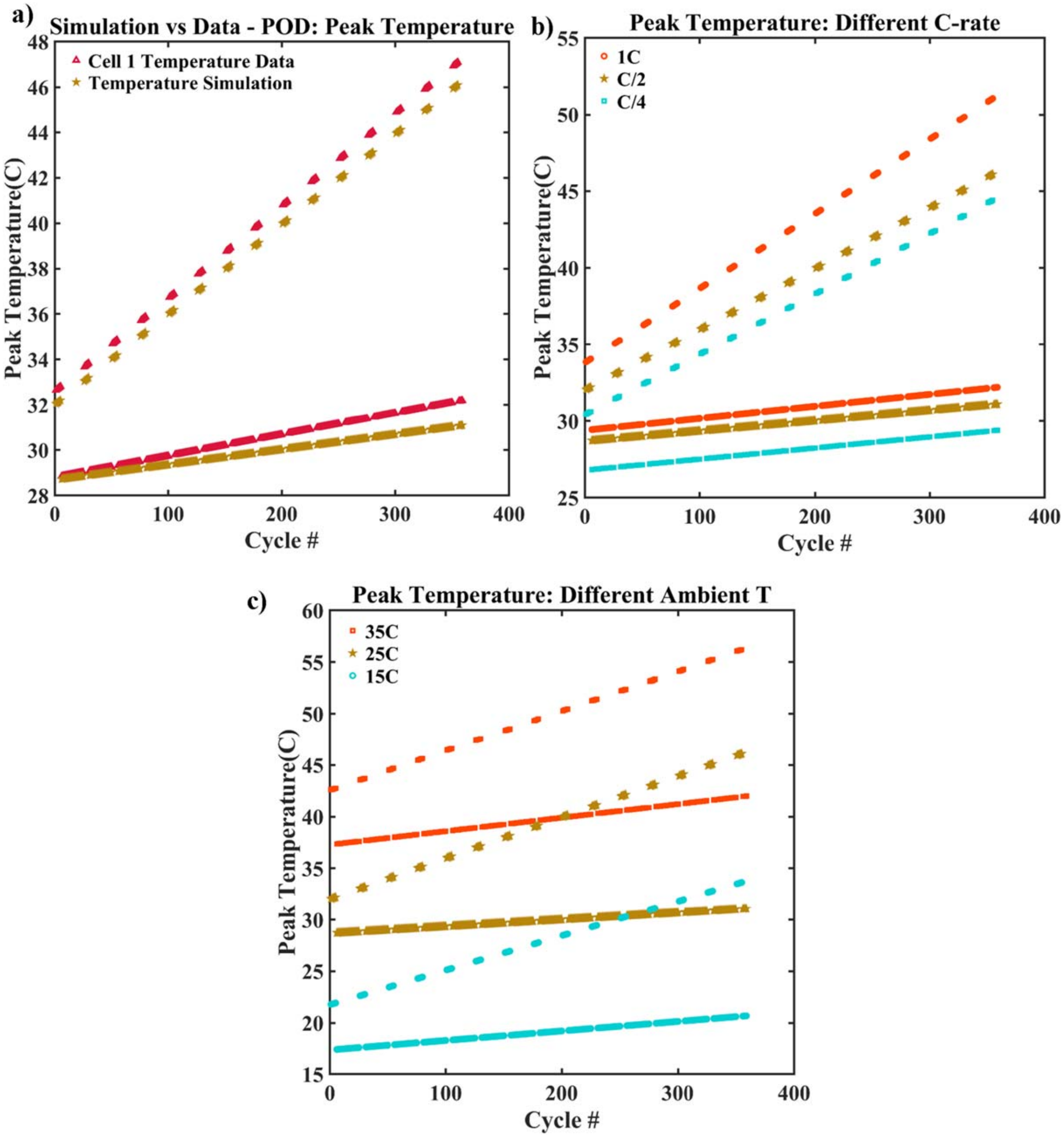

Figure 9. Peak Temperature values during discharge of Periodic over-discharge cycling (a) Model vs experimental data comparison (b) under different C-rates and (c) for different ambient temperatures.

kinetics for SEI and CEI formation as seen in Fig. 8d. This causes a much higher rate of side reactions occurring, amounting to more overall fade, thereby reducing the discharge capacity. The amount of Cu dissolution and Li plating have decreased as compared to the baseline case, which means under these conditions, the OD capacity is due to a higher voltage window, due to lower polarizations and lower side reactions occurring. Even though the fade during OD is less, the overall capacity falls below the baseline values as much of the Li inventory is lost during the normal cycling regime.

Over-discharging cells at a higher ambient temperature show higher overall fade, but more importantly, shows a higher risk for thermal runaway as seen in Fig. 9c where the peak temperature during discharge crosses 55 °C and increases with the number of cycles of operation. A few over-discharged cells in a pack under high ambient temperatures thus require a robust thermal management system to prevent the possibility of electrolyte dry-out and thermal runaway.

Model Limitation

For the given cell design keeping the over-discharge voltage stop condition the same, which is 1.5 V, we can have different behavior in the copper dissolution and deposition mechanism based on the N:P ratio of the cell. Increasing the N:P ratio would mean that the stop condition would be reached at a lower anode potential, which means lesser Cu dissolution and deposition. Decreasing the N:P ratio will increase the amount of copper dissolution and deposition as the anode potential will be higher than the current cell design case. A more detailed study on the effect of over-discharge based on cell level parameters will be analyzed in future work.

In this paper, in addition to common mechanisms for capacity fade, copper dissolution was added to the P2D model approximated with a tanks-in-series approach. Note that copper dissolution changes the architecture of the sandwich and will need a two-dimensional model with moving boundaries with careful formulation for mass conservation.[23] We hope to address the same in future publications when detailed experimental data with spatial heterogeneity becomes available.

Code Dissemination

The codes used for the plots shown in the paper are provided in MATLAB with open access for non-commercial purposes (hosted on the PI's webpage: available online at https://sites.utexas.edu/maple/models-codes-2/). The following codes are posted:

1) Single cycle simulation in the normal voltage window.
2) Single cycle simulation in the over-discharge voltage window.
3) Cycling simulations with all the capacity fade mechanisms mentioned in Table IV.

Summary

In this paper, a systematic approach was taken to develop a thermal Tanks-in-Series model to simulate over-discharge conditions for a Li-ion cell. The model was employed to study the effect and interplay of capacity fade mechanisms based on different over-discharge cycling protocols. Copper dissolution and subsequent deposition under over-discharge conditions, leading to increased SEI layer growth with subsequent cycling, explained the increasing difference in normal and over-discharge cycle capacities during periodic over-discharge. Changes in C-rate and thermal environment studies showed the tendency of lithium plating and copper dissolution to significantly affect degradation dynamics at higher rates and lower temperatures. The thermal behavior of the cell provided insights into the rise in peak over-discharge temperature during cycling which could pose a severe safety threat leading to thermal runaway.

Acknowledgments

The authors would like to acknowledge our collaborators at Electrochemical Safety Research Institute-UL Research Institutes for their discussion and insight into the effects of over-discharge on a cell and for their financial support in this project. We thank the team at Energy and Transport Sciences Lab, Purdue University for providing the experimental data shown in this paper.

Appendix

The electrode open circuit potential curves used in the manuscript are presented here as shown in Fig. A·1, along with the markers for their respective initial and final electrode SOC's as the fully charged cell is discharged, to a terminal voltage of 2.5 V and 1.5 V at the first cycle.

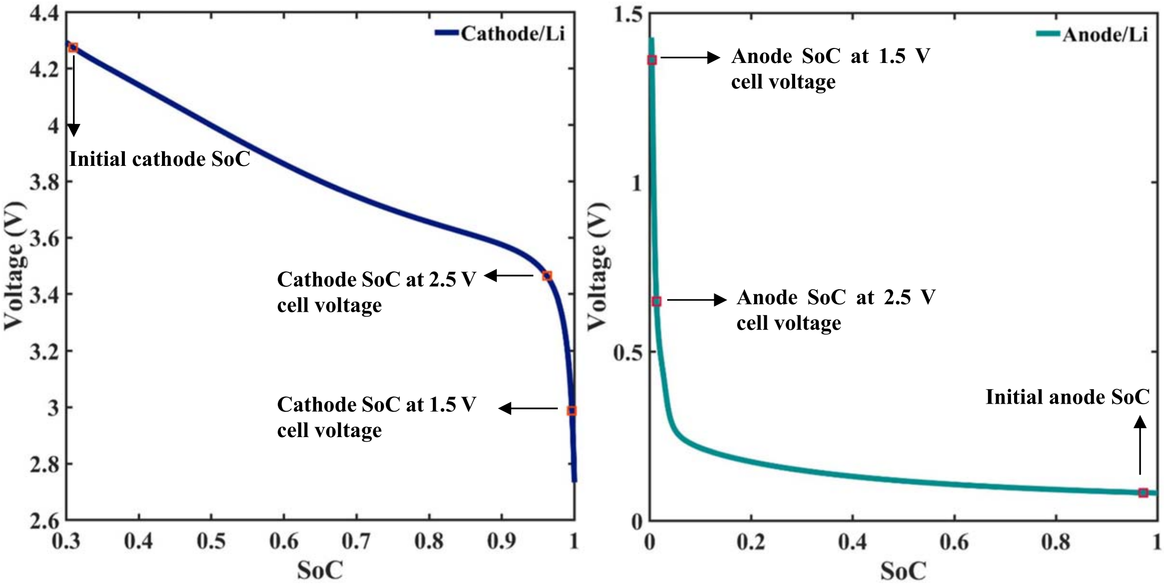

Figure A·1. OCV curves with markers of the initial SoC at the beginning of discharge, and two final SoC's at 2.5 V and 1.5 V for the (a) cathode and (b) anode.

ORCID

Raghav Sai Thiagarajan https://orcid.org/0000-0002-1535-8844
Anthony Concepción https://orcid.org/0000-0003-2694-7641
Deepti Tewari https://orcid.org/0000-0002-5573-535X
Judith A. Jeevarajan https://orcid.org/0000-0003-4843-7597
Vinay Premnath https://orcid.org/0009-0003-0314-7665
Venkat R. Subramanian https://orcid.org/0000-0002-2092-9744

References

1. UL, UL 9540 - Stand. Saf. - Energy Storage Syst. Equip. (2020).
2. IEC, IEC-62133 - Second. cells Batter. Contain. alkaline or other nonacid electrolytes—Saf. Requir. portable sealed Second. cells, Batter. made from them, use portable Appl. (2017).
3. SAE International, *J2464_202108 - Electr. Hybrid Electr. Veh. Recharg. Energy Storage Syst. Saf. Abus. Test.* (2021).
4. J. Jaguemont and F. Bardé, *Appl. Therm. Eng.*, **231**, 121014 (2023).
5. G. Zhang, X. Wei, S. Chen, J. Zhu, G. Han, and H. Dai, *J. Power Sources*, **521**, 230990 (2022).
6. C. Fear, D. Juarez-Robles, J. A. Jeevarajan, and P. P. Mukherjee, *J. Electrochem. Soc.*, **165**, A1639 (2018).
7. D. J. Robles, "Degradation-Safety Analytics in Energy Storage." *Doctoral dissertation*, Purdue University Graduate School (2019), https://doi.org/10.25394/PGS.9978782.v1.
8. C. E. Hendricks, A. N. Mansour, D. A. Fuentevilla, G. H. Waller, J. K. Ko, and M. G. Pecht, *J. Electrochem. Soc.*, **167**, 090501 (2020).
9. Z. Guo, S. Yang, W. Zhao, S. Wang, J. Liu, Z. Ma, H. Zhao, and L. Ren, *J. Energy Chem.*, **78**, 497 (2023).
10. H. Zhou, C. Fear, J. A. Jeevarajan, and P. P. Mukherjee, *Energy Storage Mater.*, **54**, 60 (2023).
11. D. Juarez-Robles, A. A. Vyas, C. Fear, J. A. Jeevarajan, and P. P. Mukherjee, *J. Electrochem. Soc.*, **167**, 090547 (2020).
12. P. Arora, R. E. White, and M. Doyle, *J. Electrochem. Soc.*, **145**, 3647 (1998).
13. E. Zsoldos, M. M. E. Cormier, N. Phattharasupakun, A. Liu, and J. R. Dahn, *J. Electrochem. Soc.*, **170**, 040511 (2023).
14. S. Erol, M. E. Orazem, and R. P. Muller, *J. Power Sources*, **270**, 92 (2014).
15. L. Li, X. Zhou, X. Ju, Z. Zhou, B. Wang, B. Cao, and L. Yang, *Appl. Therm. Eng.*, **225**, 120172 (2023).
16. H. M. Usman, S. Mukhopadhyay, and H. Rehman, *IEEE Access*, **6**, 49546 (2018).
17. A. Subramaniam, S. Kolluri, C. D. Parke, M. Pathak, S. Santhanagopalan, and V. R. Subramanian, *J. Electrochem. Soc.*, **167**, 013534 (2020).
18. A. Subramaniam, S. Kolluri, S. Santhanagopalan, and V. R. Subramanian, *J. Electrochem. Soc.*, **167**, 113506 (2020).
19. C. R. Birkl, M. R. Roberts, E. McTurk, P. G. Bruce, and D. A. Howey, *J. Power Sources*, **341**, 373 (2017).
20. X. Lin, J. Park, L. Liu, Y. Lee, A. M. Sastry, and W. Lu, *J. Electrochem. Soc.*, **160**, A1701 (2013).
21. R. S. Thiagarajan, A. Subramaniam, S. Kolluri, T. R. Garrick, Y. Preger, V. D. Angelis, J. Lim, and V. R. Subramanian, *J. Electrochem. Soc.*, **170**, 010528 (2023).
22. Z. Chen, D. L. Danilov, Q. Zhang, M. Jiang, J. Zhou, R. A. Eichel, and P. H. L. Notten, *Electrochim. Acta*, **430**, 141077 (2022).
23. T. Jang, L. Mishra, A. Subramaniam, M. Uppaluri, V. Ramadesigan, T. R. Garrick, and V. R. Subramanian, *J. Electrochem. Soc.*, **170**, 110516 (2023).